V European Conference on Computational Fluid Dynamics
ECCOMAS CFD 2010
J. C. F. Pereira and A. Sequeira (Eds)
Lisbon, Portugal,14-17 June 2010

# APPLICATION OF A DISCONTINUOUS CHARACTERISTIC BASED SPLIT SCHEME FOR FLUID-STRUCTURE INTERACTION

**Ralf Unger*, Matthias C. Haupt* and Peter Horst***

*Institute of Aircraft Design and Lightweight Structures,
Technische Universität Braunschweig
Hermann-Blenk-Str. 35
38108 Braunschweig, Germany
r.unger, m.haupt, p.horst@tu-braunschweig.de

**Key words:** Characteristic based split, Discontinuous Galerkin, Finite element method, Fluid-structure interaction, Aeroelasticity, Panel flutter

**Abstract.** *In this paper, the arbitrary Lagrangian Eulerian (ALE) form of the compressible Navier-Stokes equations are treated with the characteristic based split scheme. A weak integral statement of the resulting equations is obtained by introducing weight functions. A local conservative scheme can be designed by a proper integration by parts and discretization for each finite element. This removes the standard finite element assembly, necessary for the global Galerkin scheme and the element-by-element linking is considered by the elemental edge flux, which is explicitly treated locally conservative. Since for each finite element a matrix system is computed and solved independently, this discontinuous characteristic based split scheme can be easily parallelized.*

*As a numerical example for fluid structure interaction, the classical panel flutter problem is investigated. The discontinuous characteristic based split scheme is incorporated in a flexible coupling environment together with a finite element procedure for the structure as well as a finite element transfer and grid deformation scheme. Results and comparison with the global Galerkin scheme show the applicability and accuracy of the discontinuous characteristic based split scheme.*

## 1 INTRODUCTION

Within the field of Computational Fluid Dynamics (CFD), a major method of solving the governing fluid equations is the finite element method. The finite element method for fluid flow problems was established in the last twenty years, while first attempts were made by Zienkiewicz, [1], Oden, [2], or Chung, [3]. To use the standard Petrov-Galerkin form (weight functions are equal to interpolation functions), stability schemes need to be used to suppress instabilities caused by the convective terms of the fluid equations. Such stability terms are introduced naturally by the characteristic based split scheme proposed by Zienkiewicz and Codina [4, 5], which use a local Taylor expansion to design a computational effective scheme. A good overview of this scheme is given by Nithiarasu in [6] and nowadays the CBS scheme is widely used to solve the compressible and incompressible fluid flows. In this paper, the CBS scheme from [6] is modified and extended to the Navier-Stokes equation in the arbitrary Eulerian-Lagrange (ALE) frame of reference to take aeroelastic problems into account.

In [4], mass matrix lumping was proposed to design a matrix free solution method. However, using the standard CBS scheme in conjunction with higher order finite elements, e.g. biquadratic quadrilateral finite elements, mass matrix lumping is not applicable, due to the appearance of unphysical oscillations caused by the nodal decoupling. Further and as noted in [7], the usage of mass matrix lumping can lead to serious errors when used for transient problems. Therefore a consistent mass matrix should be applied in such situations, which however is computational expensive with many degrees of freedom. Alternatively, an elemental discontinuous Galerkin form of the CBS scheme can be used, which was proposed for incompressible fluid flow problems in [8, 9].

The discontinuous Galerkin method has been developed mainly for problems in fluid mechanics and combine features of the finite element and the finite volume schemes. A good overview of this methodology can be found in [10, 11] and the references therein. One important advantage of the discontinuous Galerkin method is the possibility of easy parallelization of the algorithm since this method allows an element by element solution procedure. However, each node belongs to several elements and therefore multiple solutions for each node need to be stored, which results in a large memory requirement. Further, additional edge fluxes for each element have to be computed, which makes the discontinuous methodology more computational expensive than its continuous Galerkin counterpart.

In this paper, a discontinuous characteristic based split scheme for the ALE frame of reference is employed, which has the same structure as the continuous Galerkin form of the CBS scheme. This has the advantages, that only minor modifications to the CBS scheme are necessary and that computational effort is reduced, [12]. The standard finite element assembly of the continuous Galerkin form is removed and the element by element linking is done by the edge flux, which ensures continuity between the elements. This edge flux also can be used to satisfy a local or elemental conservation, if this flux is equal for the common boundary of two adjoining elements. Due to the avoiding of a global matrix system, the necessity of solving a system of linear algebraic equation is omitted.

The remainder of the paper is organized as follows. In section 2, the discontinuous characteristic based split for the ALE frame of reference is introduced by first recapitulating the standard global continuous Galerkin CBS scheme. In section 3, this scheme is verified by comparing

the stationary fluid flow around the NACA0012 airfoil using the continuous and discontinuous version of the CBS scheme. Here also higher order finite elements are involved, which is an improvement to examples given in [6, 7], where only linear triangular elements were used. In section 4, the three field coupling approach is introduced, which is then applied for the coupled aeroelastic computation of the transonic panel flutter problem conducted in section 5.

## 2 DISCONTINUOUS CHARACTERISTIC BASED SPLIT SCHEME

The CBS scheme uses a local Taylor expansion to design a computational effective procedure and a good overview of this scheme is given by Nithiarasu in [6] Nowadays, the CBS method with a subsequent spatial discretization is widely used to solve the compressible and incompressible fluid flows and the third volume of the well-known book set [7] covers the CBS scheme for fluid dynamics in great detail. Before introducing the discontinuous characteristic based split scheme, the global continuous Galerkin form of the CBS scheme will be written for the arbitrary Lagrangian Eulerian (ALE) form of the Navier-Stokes equation.

### 2.1 Global continuous Galerkin Form of the Characteristic Based Split Scheme

With the conservative variables $\boldsymbol{V} = \rho\boldsymbol{v}$ and $E = \rho e$, the non-dimensional form of the conservative compressible Navier-Stokes equation in the ALE frame of reference can be written as:

- equation of mass conservation:

$$\frac{\partial \rho}{\partial t} + \nabla^T \boldsymbol{V} - \boldsymbol{w}^T \nabla \rho = 0 \tag{1}$$

- equation of momentum conservation:

$$\frac{\partial \boldsymbol{V}}{\partial t} + [\nabla^T(\boldsymbol{v}\boldsymbol{V}^T)]^T - [\boldsymbol{w}^T \nabla \boldsymbol{V}^T]^T = -\nabla p + \frac{1}{Re}\boldsymbol{\mathcal{D}}^T\boldsymbol{\tau} + \rho\hat{\boldsymbol{b}} \tag{2}$$

- equation of energy conservation:

$$\frac{\partial E}{\partial t} + \nabla^T(\boldsymbol{v}E) - \boldsymbol{w}^T\nabla E = -\nabla^T(p\boldsymbol{v}) + \frac{1}{Re}\nabla^T(\boldsymbol{Q}^T\boldsymbol{\tau}) + \frac{1}{Re\,Pr}\nabla^T(\kappa\nabla T) + \rho\hat{\boldsymbol{b}}^T\boldsymbol{v}\,, \tag{3}$$

where $\rho$, $\boldsymbol{v}$, $e$, $p$, $T$ and $t$ is the fluid density, the velocity, the specific total energy, the pressure, the temperature and the time, respectively. The vector $\boldsymbol{w}$ is the velocity of the ALE frame of reference expressed in the Eulerian frame of reference. In vector notation, the viscous stress vector $\boldsymbol{\tau}$ is written as:

$$\boldsymbol{\tau} = \mu\left(\boldsymbol{I}_0 - \frac{2}{3}\boldsymbol{m}\boldsymbol{m}^T\right)\boldsymbol{\mathcal{D}}\boldsymbol{v}\,, \tag{4}$$

with a diagonal and a operator matrix, $\boldsymbol{I}_0$ and $\boldsymbol{\mathcal{D}}$:

$$\boldsymbol{I}_0 = \begin{bmatrix} 2 & 0 & 0 & 0 & 0 & 0 \\ 0 & 2 & 0 & 0 & 0 & 0 \\ 0 & 0 & 2 & 0 & 0 & 0 \\ 0 & 0 & 0 & 1 & 0 & 0 \\ 0 & 0 & 0 & 0 & 1 & 0 \\ 0 & 0 & 0 & 0 & 0 & 1 \end{bmatrix} \quad \boldsymbol{\mathcal{D}}^T = \begin{bmatrix} \frac{\partial}{\partial x_1} & 0 & 0 & \frac{\partial}{\partial x_2} & 0 & \frac{\partial}{\partial x_3} \\ 0 & \frac{\partial}{\partial x_2} & 0 & \frac{\partial}{\partial x_1} & \frac{\partial}{\partial x_3} & 0 \\ 0 & 0 & \frac{\partial}{\partial x_3} & 0 & \frac{\partial}{\partial x_2} & \frac{\partial}{\partial x_1} \end{bmatrix}$$

and $\boldsymbol{m}^T = [1,1,1,0,0,0]$ gives the functionality of the Kronecker delta to the stress vector. External body forces per mass unit are given by the vector $\hat{\boldsymbol{b}}$. $\boldsymbol{Q}$ is a 6x3 matrix, which has the same structure as $\boldsymbol{\mathcal{D}}$ but contains the fluid velocities as:

$$\boldsymbol{Q}^T = \begin{bmatrix} v_1 & 0 & 0 & v_2 & 0 & v_3 \\ 0 & v_2 & 0 & v_1 & v_3 & 0 \\ 0 & 0 & v_3 & 0 & v_2 & v_1 \end{bmatrix}.$$

Finally, the values for viscosity, $\mu$, and the thermal conductivity, $\kappa$, are a function of the temperature. For air these values are given by Sutherland's relation through, [13]:

$$\begin{gathered} \frac{\mu}{\mu_0} = \left(\frac{T}{T_0}\right)^{\frac{3}{2}} \frac{T_0 + S_\mu}{T + S_\mu} \quad \text{and} \quad \frac{\kappa}{\kappa_0} = \left(\frac{T}{T_0}\right)^{\frac{3}{2}} \frac{T_0 + S_k}{T + S_k} \\ T_0 = 273.15\,\mathrm{K}, \quad \mu_0 = 1.7161 \cdot 10^{-5}\,\tfrac{\mathrm{kg}}{\mathrm{m\,s}}, \quad \kappa_0 = 2.3360 \cdot 10^{-2}\,\tfrac{\mathrm{J}}{\mathrm{m\,s\,K}}, \\ S_\mu = 110.4\,\mathrm{K}, \quad S_\kappa = 112.0\,\mathrm{K}\,, \end{gathered} \tag{5}$$

where $S$ is called Sutherland temperature, which is slightly different for the viscosity and conductivity expression. The Reynolds and Prandtl number are a results of the non-dimensionalization and introduced as:

$$Re = \frac{\rho_\infty v_\infty l}{\mu_\infty} \quad Pr = \frac{\mu_\infty c_p}{\kappa_\infty}\,. \tag{6}$$

The value $c_p$ is the specific heat at constant pressure and $l$ is a reference length.

The fluid quantities are spatially discretized by a shape function interpolation as:

$$\begin{aligned} &\rho \approx \mathbf{N}\boldsymbol{\rho}; \qquad p \approx \mathbf{N}\mathbf{p}; \qquad \boldsymbol{v} \approx \mathbf{N}_v\mathbf{v}; \qquad \boldsymbol{w} \approx \mathbf{N}_v\mathbf{w}; \\ &\boldsymbol{s} \approx \mathbf{N}_v\mathbf{s}; \qquad \boldsymbol{V} \approx \mathbf{N}_v\mathbf{V}; \qquad E \approx \mathbf{N}\mathbf{E}; \qquad T \approx \mathbf{N}\mathbf{T}; \end{aligned} \tag{7}$$

where $\mathbf{N} = [\mathsf{N}_1, \mathsf{N}_2, \ldots, \mathsf{N}_m]$ are the vector of shape functions at the nodes with $m$ being the number of nodes and $\boldsymbol{\rho}$, $\mathbf{p}$, $\mathbf{E}$ and $\mathbf{T}$ denote the vector form of the particular fluid quantity. Each component of the fluid velocity is approximated with the shape functions as used for each other fluid quantity and thus:

$$\mathbf{N}_v = \begin{bmatrix} \mathsf{N}_1 & 0 & 0 & \mathsf{N}_2 & 0 & 0 & \ldots & \mathsf{N}_m & 0 & 0 \\ 0 & \mathsf{N}_1 & 0 & 0 & \mathsf{N}_2 & 0 & \ldots & 0 & \mathsf{N}_m & 0 \\ 0 & 0 & \mathsf{N}_1 & 0 & 0 & \mathsf{N}_2 & \ldots & 0 & 0 & \mathsf{N}_m \end{bmatrix}$$
$$\mathbf{V} = [\mathsf{V}_{11}, \mathsf{V}_{12}, \mathsf{V}_{13}, \mathsf{V}_{21}, \mathsf{V}_{22}, \mathsf{V}_{23} \ldots, \mathsf{V}_{m1}, \mathsf{V}_{m2}, \mathsf{V}_{m3}]^T$$

The velocity $\boldsymbol{s}$ is the so-called convective velocity, simply calculated as $\boldsymbol{s} = \boldsymbol{v} - \boldsymbol{w}$. With this spatial discretization and similar to the Navier-Stokes equation in a fixed Eulerian frame of reference, see [7], Eq. (1) to (3) can be temporally treated with a global continuous CBS scheme resulting in the following matrix system (without body forces):

1. solve an intermediate velocity $\Delta\check{\mathbf{V}}$

$$\Delta\check{\mathbf{V}} = \mathbf{M}_v^{-1}\Delta t\Big[(-\mathbf{C}_{sV}\mathbf{V} - \mathbf{K}_\tau\mathbf{v} + \mathbf{f}_\tau) + \Delta t(-\mathbf{K}_{sV}\mathbf{V} - \mathbf{K}_{pV}\mathbf{p})\Big]^n, \tag{8}$$

where:

$$\mathbf{M}_v = \int_\Omega \mathbf{N}_v^T\mathbf{N}_v\, d\Omega; \quad \mathbf{K}_\tau = \int_\Omega \mathbf{B}_\tau^T \frac{\mu}{Re}\left(\boldsymbol{I}_0 - \tfrac{2}{3}\boldsymbol{m}\boldsymbol{m}^T\right)\mathbf{B}_\tau\, d\Omega;$$

$$\mathbf{C}_{sV} = \int_\Omega \mathbf{N}_v^T\mathbf{B}_s\, d\Omega; \qquad \mathbf{f}_\tau = \int_\Gamma \mathbf{N}_v^T\boldsymbol{\Upsilon}^T\left[\frac{\mu}{Re}\left(\boldsymbol{I}_0 - \tfrac{2}{3}\boldsymbol{m}\boldsymbol{m}^T\right)\mathbf{B}_\tau\mathbf{v}\right] d\Gamma;$$

$$\mathbf{K}_{sV} = \frac{1}{2}\int_\Omega \mathbf{B}_s^T\mathbf{B}_s\, d\Omega; \qquad \mathbf{K}_{pV} = \frac{1}{2}\int_\Omega \mathbf{B}_s^T(\nabla\mathbf{N})\, d\Omega;$$

The $\mathbf{B}$-matrices are expressed as:

$$\mathbf{B}_s = \begin{bmatrix} \mathsf{b}_{s1} & 0 & 0 & \mathsf{b}_{s2} & 0 & 0 & \dots & \mathsf{b}_{sm} & 0 & 0 \\ 0 & \mathsf{b}_{s1} & 0 & 0 & \mathsf{b}_{s2} & 0 & \dots & 0 & \mathsf{b}_{sm} & 0 \\ 0 & 0 & \mathsf{b}_{s1} & 0 & 0 & \mathsf{b}_{s2} & \dots & 0 & 0 & \mathsf{b}_{sm} \end{bmatrix}; \quad \mathsf{b}_{si} = \mathbf{s}_i^T(\nabla\mathsf{N}_i)$$

$$\mathbf{B}_\tau = \mathcal{D}\mathbf{N}_v;$$

The matrix $\boldsymbol{\Upsilon}^T$ contains the entries of the boundary normal vector:

$$\boldsymbol{\Upsilon}^T = \begin{bmatrix} n_1 & 0 & 0 & n_2 & 0 & n_3 \\ 0 & n_2 & 0 & n_1 & n_3 & 0 \\ 0 & 0 & n_3 & 0 & n_2 & n_1 \end{bmatrix} \tag{9}$$

2. solve the pressure $\Delta\mathbf{p}$

$$\Delta\mathbf{p} = (\mathbf{M}_p + \Delta t^2\theta_1\theta_2\mathbf{K}_p)^{-1}\Delta t\Big[\mathbf{G}(\mathbf{V}^n + \theta_1\Delta\check{\mathbf{V}}) + \mathbf{C}_{w\rho}\boldsymbol{\rho}^n - \mathbf{f}_V + \Delta t\theta_1(-\mathbf{K}_p\mathbf{p}^n + \mathbf{f}_p)\Big], \tag{10}$$

where:

$$\mathbf{M}_p = \int_\Omega \mathbf{N}^T\left(\frac{1}{c^2}\right)^n\mathbf{N}\, d\Omega; \quad \mathbf{K}_p = \int_\Omega (\nabla\mathbf{N})^T(\nabla\mathbf{N})\, d\Omega;$$

$$\mathbf{G} = \int_\Omega (\nabla\mathbf{N})^T\mathbf{N}_v\, d\Omega; \quad \mathbf{f}_p = \int_\Gamma \mathbf{N}^T(\nabla\mathbf{N}\mathbf{p}^n)^T\boldsymbol{n}\, d\Gamma; \quad \mathbf{C}_{w\rho} = \int_\Omega \mathbf{N}^T\mathbf{L}_w\, d\Omega;$$

$$\mathbf{f}_V = \int_\Gamma \mathbf{N}^T(\mathbf{N}_v[\mathbf{V}^n + \theta_1\Delta\check{\mathbf{V}}])^T\boldsymbol{n}\, d\Gamma; \quad \mathbf{L}_w = [\mathsf{b}_{w1}, \mathsf{b}_{w2}, \dots, \mathsf{b}_{wm}]; \quad \mathsf{b}_{wi} = \mathbf{w}_i^T(\nabla\mathsf{N}_i);$$

where $\theta_1$ and $\theta_2$ are user-defined relaxation parameters, which are set to $\theta_1 = 0.75$, $\theta_2 = 0.0$ (explicit version). The quantity $c$ denotes the speed of sound.

3. correct velocity $\Delta\mathbf{V}$

$$\Delta\mathbf{V} = \Delta\check{\mathbf{V}} + \mathbf{M}_v^{-1}\Delta t\Big[-\mathbf{G}^T(\mathbf{p}^n + \theta_2\Delta\mathbf{p})\Big]. \tag{11}$$

4. solve energy equation $\Delta\mathbf{E}$

$$\Delta\mathbf{E} = \mathbf{M}^{-1}\Delta t\Big[(-\mathbf{C}_{sE}\mathbf{E} - \mathbf{C}_{vE}\mathbf{p} - \mathbf{K}_{\tau E}\mathbf{v} - \mathbf{K}_T\mathbf{T} + \mathbf{f}_E) + \Delta t(-\mathbf{K}_{sE}\mathbf{E} - \mathbf{K}_{vE}\mathbf{p})\Big]^n, \tag{12}$$

with the matrices and vectors:

$$\mathbf{C}_{sE} = \int_\Omega \mathbf{N}^T\mathbf{L}_s\,d\Omega; \quad \mathbf{C}_{vE} = \int_\Omega \mathbf{N}^T\mathbf{L}_v\,d\Omega; \quad \mathbf{K}_T = \int_\Omega (\nabla\mathbf{N})^T\frac{\kappa}{Re\,Pr}(\nabla\mathbf{N})\,d\Omega;$$

$$\mathbf{K}_{\tau E} = \int_\Omega (\nabla\mathbf{N})^T\boldsymbol{Q}^T\frac{\mu}{Re}\left(\boldsymbol{I}_0 - \tfrac{2}{3}\boldsymbol{m}\boldsymbol{m}^T\right)\mathbf{B}_\tau\,d\Omega; \quad \mathbf{K}_{sE} = \frac{1}{2}\int_\Omega \mathbf{L}_s^T\mathbf{L}_s\,d\Omega;$$

$$\mathbf{f}_E = \int_\Gamma \mathbf{N}^T\frac{1}{Re}\left(\boldsymbol{Q}^T\left[\mu\left(\boldsymbol{I}_0 - \tfrac{2}{3}\boldsymbol{m}\boldsymbol{m}^T\right)\mathbf{B}_\tau\mathbf{v}\right] + \frac{\kappa}{Pr}(\nabla\mathbf{N})\mathbf{T}\right)^T\boldsymbol{n}\,d\Gamma;$$

$$\mathbf{M} = \int_\Omega \mathbf{N}^T\mathbf{N}\,d\Omega; \quad \mathbf{K}_{vE} = \frac{1}{2}\int_\Omega \mathbf{L}_s^T\mathbf{L}_v\,d\Omega; \quad \mathbf{L}_s = [\mathsf{b}_{s1}, \mathsf{b}_{s2}, \ldots, \mathsf{b}_{sm}];$$

$$\mathbf{L}_v = [\mathsf{b}_{v1}, \mathsf{b}_{v2}, \ldots, \mathsf{b}_{vm}]; \quad \mathsf{b}_{vi} = \mathbf{v}_i^T(\nabla\mathsf{N}_i); \quad \mathsf{b}_{si} = \mathbf{s}_i^T(\nabla\mathsf{N}_i);$$

All additional tools like mass matrix lumping, variable smoothing, artificial compressibility, shock capturing, local time stepping can be used here, [6]. In contrast to the original proposed scheme, the term $\mathbf{K}_{pV}\mathbf{p}$ is here evaluated within the first step instead of the third step. With the above algorithm a solution is iterated to steady state and unsteady solution can be obtained with the well-known dual-time stepping approach, [14]. The grid velocity $\mathbf{w}$ is calculated, so that the geometric conservation law is satisfied, [15].

### 2.2 Discontinuous Galerkin form

As noted in [7], the usage of mass matrix lumping within the equations Eq. (8) to (12) can lead to serious errors when used for transient problems. Further, it could be observed, that unphysical oscillations appear in the solution, when mass matrix lumping is applied for quadratic and higher order elements, i.e. elements with quadratic and higher order shape function interpolation. Such oscillations result from the nodal decoupling when a lumped mass matrix is used. Therefore a consistent mass matrix should be applied in such situations, which however is computational expensive with many degrees of freedom. Alternatively, an elemental discontinuous Galerkin form of the CBS scheme can be used, which was proposed for incompressible fluid flow problems in [9].

Here, a discontinuous CBS scheme for the ALE frame of reference is now employed, which has the same structure as the continuous Galerkin form of the CBS scheme. That has the advantages, that only minor modifications to the CBS scheme are necessary and that computational effort is

reduced, [12]. The standard finite element assembly of the continuous Galerkin form is removed and the element by element linking is done by the edge flux, which ensures continuity between the elements. This edge flux also can be used to satisfy a local or elemental conservation, if this flux is equal for the common boundary of two adjoining elements. Due to the avoiding of a global matrix system, the necessity of solving a system of linear algebraic equation is omitted. A noted in [9], the discontinuous CBS scheme is not only globally but also locally conservative in terms of the fluid variables, which is important especially for incompressible flow problems.

The discontinuous Galerkin form of the CBS scheme starts with the same weak statement as continuous Galerkin form but an additional integration by parts for all convective terms is applied, which yields in the appearance of an additional edge flux. Thus, for *each* finite element $\Omega^e$ the following matrix system has to be solved in each time step:

1. solve an intermediate velocity step $\Delta\check{\mathbf{V}}$

$$\Delta\check{\mathbf{V}} = \mathbf{M}_v^{e,-1}\Delta t\Big[(\mathbf{C}_{sV}^e\mathbf{V} - \mathbf{K}_\tau^e\mathbf{v} - \mathbf{f}_{sV}^e + \mathbf{f}_\tau^e) + \Delta t(-\mathbf{K}_{sV}^e\mathbf{V} - \mathbf{K}_{pV}^e\mathbf{p})\Big]^n, \tag{13}$$

where

$$\mathbf{M}_v^e = \int_{\Omega^e}\mathbf{N}_v^T\mathbf{N}_v\,d\Omega^e; \qquad \mathbf{C}_{sV}^e = \int_{\Omega^e}\mathbf{B}_s^T\mathbf{N}_v\,d\Omega^e; \qquad \mathbf{K}_{sV}^e = \frac{1}{2}\int_{\Omega^e}\mathbf{B}_s^T\mathbf{B}_s\,d\Omega^e$$

$$\mathbf{K}_\tau^e = \int_{\Omega^e}\mathbf{B}_\tau^T\frac{\mu}{Re}\left(\boldsymbol{I}_0 - \tfrac{2}{3}\boldsymbol{m}\boldsymbol{m}^T\right)\mathbf{B}_\tau\,d\Omega^e; \qquad \mathbf{f}_\tau^e = \int_{\Gamma^e}\frac{1}{Re}\mathbf{N}_v^T\boldsymbol{\Upsilon}^T\mathbf{N}_\tau\acute{\boldsymbol{\tau}}\,d\Gamma^e;$$

$$\mathbf{f}_{sV}^e = \int_{\Omega^e}\mathbf{N}_v^T(\boldsymbol{s}^T\boldsymbol{n})\mathbf{N}_v\mathbf{V}\,d\Gamma^e; \qquad \mathbf{K}_{pV}^e = \frac{1}{2}\int_{\Omega^e}\mathbf{B}_s^T(\nabla\mathbf{N})\,d\Omega^e;$$

It is imported to note, that for the boundary term $\mathbf{f}_\tau^e$ the nodal stress vector $\acute{\boldsymbol{\tau}}$ is needed, which is spatial interpolated with the shape function matrix $\mathbf{N}_\tau$. This form ensures the local conservation of the edge flux and requires the nodal stress values to be computed in an additional post-processing step in each iteration. Further, the difference of $\mathbf{C}_{sV}^e$ and $\mathbf{C}_{sV}$ on element level should be pointed out.

2. solve the pressure $\Delta\mathbf{p}$

$$\Delta\mathbf{p} = (\mathbf{M}_p^e + \Delta t^2\theta_1\theta_2\mathbf{K}_p^e)^{-1}\Delta t\Big[\mathbf{G}_V^e(\mathbf{V}^n + \theta_1\Delta\check{\mathbf{V}}) + \mathbf{C}_{w\rho}^e\boldsymbol{\rho}^n - \mathbf{f}_V^e + \Delta t\theta_1(-\mathbf{K}_p^e\mathbf{p}^n + \mathbf{f}_p^e)\Big], \tag{14}$$

where

$$\mathbf{M}_p^e = \int_{\Omega^e}\mathbf{N}^T\left(\frac{1}{c^2}\right)^n\mathbf{N}\,d\Omega^e; \quad \mathbf{K}_p^e = \int_{\Omega^e}(\nabla\mathbf{N})^T(\nabla\mathbf{N})\,d\Omega^e; \quad \mathbf{G}_V^e = \int_{\Omega^e}(\nabla\mathbf{N})^T\mathbf{N}_v\,d\Omega^e;$$

$$\mathbf{f}_p^e = \int_{\Gamma^e}\mathbf{N}^T\boldsymbol{n}^T\mathbf{N}_v\mathbf{p}_{f,\boldsymbol{x}}\,d\Gamma^e; \ \mathbf{C}_{w\rho}^e = \int_{\Omega^e}\mathbf{N}^T\mathbf{L}_w\,d\Omega^e; \ \mathbf{f}_V^e = \int_{\Gamma^e}\mathbf{N}^T(\mathbf{N}_v[\mathbf{V}^n + \theta_1\Delta\check{\mathbf{V}}])^T\boldsymbol{n}\,d\Gamma^e;$$

Similar to the vector $\mathbf{f}_\tau^e$ from step 1, the nodal pressure derivatives $\mathbf{p}_{f,\boldsymbol{x}}$ interpolated with $\mathbf{N}_v$ are needed for the $\mathbf{f}_p^e$ to ensure local conservation over the element boundaries. This nodal pressure derivatives are calculated in an extra step in each iteration.

3. correct velocity $\Delta\mathbf{V}$

$$\Delta\mathbf{V} = \Delta\check{\mathbf{V}} + \mathbf{M}_v^{e,-1}\Delta t\left[\mathbf{G}_p^e(\mathbf{p}^n + \theta_2\Delta\mathbf{p}) - \mathbf{f}_{V2}^e\right]. \tag{15}$$

where again integration by parts was used to obtain the elemental boundary flux $\mathbf{f}_{V2}^e$ The matrices and vectors are defined as:

$$\mathbf{G}_p^e = \int_{\Omega^e}\left(\begin{bmatrix}\partial/\partial x_1 & 0 & 0\\ 0 & \partial/\partial x_2 & 0\\ 0 & 0 & \partial/\partial x_3\end{bmatrix}\mathbf{N}_v\right)^T\mathbf{N}\,d\Omega^e; \qquad \mathbf{f}_{V2}^e = \int_{\Gamma^e}\mathbf{N}_v^T\boldsymbol{n}\mathbf{N}\mathbf{p}^n\,d\Gamma^e;$$

4. solve energy equation $\Delta\mathbf{E}$

$$\begin{aligned}\Delta\mathbf{E} = \mathbf{M}^{e,-1}\Delta t\Big[&(\mathbf{C}_{sE}^e\mathbf{E} + \mathbf{C}_{vE}^e\mathbf{p} - \mathbf{K}_{\tau E}^e\mathbf{v} - \mathbf{K}_T^e\mathbf{T} - \mathbf{f}_{sE}^e - \mathbf{f}_{vE}^e + \mathbf{f}_E^e)\\ &+ \Delta t(-\mathbf{K}_{sE}^e\mathbf{E} - \mathbf{K}_{vE}^e\mathbf{p})\Big]^n,\end{aligned} \tag{16}$$

with the matrices and vectors being:

$$\mathbf{C}_{sE}^e = \int_{\Omega^e}\mathbf{L}_s^T\mathbf{N}\,d\Omega^e; \quad \mathbf{C}_{vE}^e = \int_{\Omega^e}\mathbf{L}_v^T\mathbf{N}\,d\Omega^e; \quad \mathbf{K}_{sE}^e = \frac{1}{2}\int_{\Omega^e}\mathbf{L}_s^T\mathbf{L}_s\,d\Omega^e;$$

$$\mathbf{K}_{vE}^e = \frac{1}{2}\int_{\Omega^e}\mathbf{L}_s^T\mathbf{L}_v\,d\Omega^e; \quad \mathbf{K}_T^e = \int_{\Omega^e}(\nabla\mathbf{N})^T\frac{\kappa}{Re\,Pr}(\nabla\mathbf{N})\,d\Omega^e;$$

$$\mathbf{f}_{vE}^e = \int_{\Omega^e}\mathbf{N}^T(\boldsymbol{v}^T\boldsymbol{n})\mathbf{N}\mathbf{p}\,d\Gamma^e; \quad \mathbf{K}_{\tau E}^e = \int_{\Omega^e}(\nabla\mathbf{N})^T\boldsymbol{Q}^T\frac{\mu}{Re}\left(\boldsymbol{I}_0 - \tfrac{2}{3}\boldsymbol{m}\boldsymbol{m}^T\right)\mathbf{B}_\tau\,d\Omega^e;$$

$$\mathbf{f}_{sE}^e = \int_{\Omega^e}\mathbf{N}^T(\boldsymbol{s}^T\boldsymbol{n})\mathbf{N}\mathbf{E}\,d\Gamma^e; \quad \mathbf{f}_E^e = \int_{\Gamma^e}\mathbf{N}^T\frac{\boldsymbol{n}}{Re}\left(\boldsymbol{Q}^T\mathbf{N}_\tau\acute{\boldsymbol{\tau}} + \frac{\kappa}{Pr}\mathbf{N}_v\mathbf{T}_{f,\boldsymbol{x}}\right)\,d\Gamma^e;$$

Again, the nodal temperature derivative $\mathbf{T}_{f,\boldsymbol{x}}$ are needed for the element boundary flux to ensure local conservation and this vector is computed at the end of each iteration cycle.

### 2.3 Calculation of the edge fluxes and continuous solution

As already mentioned above, the discontinuous CBS scheme ensures a conservation of the flux crossing a common boundary of neighboring elements. In Figure 1, a triangular (e1) and a quadrilateral (e2) element are depicted, which share a common edge. The condition for this flux conservation can be expressed with the aid of the boundary normals as:

$$\mathbf{F}_{e1}^T\boldsymbol{n}_{e1} = \mathbf{F}_{e2}^T\boldsymbol{n}_{e2}\,, \tag{17}$$

where $\mathbf{F}_{ei}$ is the flux and $\boldsymbol{n}_{ei}$ denotes the outward normal of the common boundary. Due to this equation, nodal values of the viscous stress vector and of the pressure and temperature derivatives are necessary, which are calculated from the surrounding elements of the node in

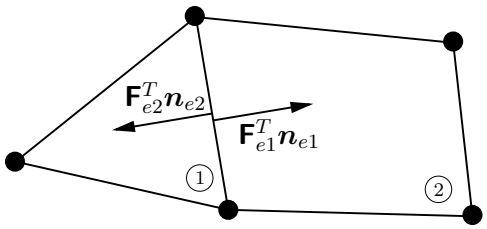


Figure 1: Triangular and Quadrilateral element sharing a common boundary, where the flux is conserved

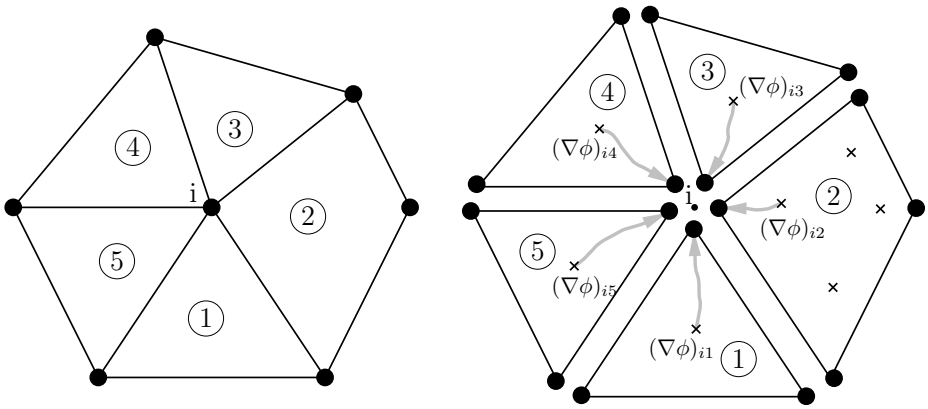


Figure 2: Patch of 5 finite elements and its discontinuous discretization - calculation of the a nodal derivatives $(\nabla\phi)_i$

question once a global continuous solution is obtained. For triangular elements these derivatives are constant for each element and a mean value for the node can be computed straightforward. For quadrilateral elements and higher order elements, the derivatives are extrapolated from the Gaussian points of the element to the node and the nodal derivative is obtained by averaging these elemental derivatives. In Figure 2, a patch of $N_{ie} = 5$ elements is shown and the nodal derivatives $(\nabla\phi)_i$ at a node $i$ is calculated as:

$$(\nabla\phi)_i = \frac{1}{N_{ie}} \sum_{e=1}^{N_{ie}} (\nabla\phi)_{ei} \,. \tag{18}$$

In a similar way, the global continuous solution $(\mathbf{p}, \mathbf{V}, \mathbf{E})$ is obtained by averaging the local elemental solution at the node in question, that is:

$$\phi_i = \frac{1}{N_{ie}} \sum_{e=1}^{N_{ie}} \phi_{ei} \,, \tag{19}$$

where $\phi_i$ is the global discrete solution at the node $i$ and $\phi_{ei}$ the solution at the node $i$ on element level.

After obtaining the global continuous solution, the calculation of the secondary fluid quantities like temperature, local Mach-Number, etc. is accomplished. Further, the variable smoothing

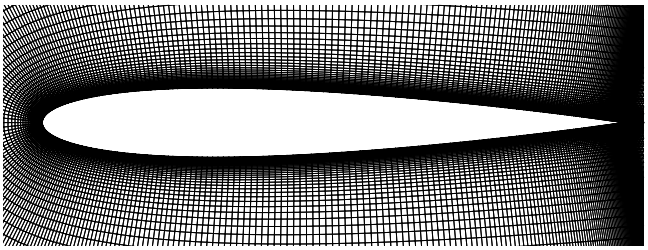

Figure 3: Structured grid for calculation of laminar viscous flow past the NACA0012 airfoil - level 0

procedure or the shock capturing scheme can be conducted. For incompressible flow problems, the artificial compressibility scheme is available without restriction. A transient solution can again be recovered by the dual time-stepping approach.

## 3 VERIFICATION OF THE DISCONTINUOUS CBS SCHEME

In this section, both forms of the CBS scheme - continuous and discontinuous Galerkin - are compared for an example of pure fluid motion on fixed grids, i.e. $\boldsymbol{w} = \boldsymbol{0}$ and $\boldsymbol{s} = \boldsymbol{v}$. The fluid flow past a NACA0012 airfoil is investigated for a free stream Mach number of $Ma_\infty = 0.85$, a Reynolds number of $Re = 2000$ and an angle of attack of $\alpha = 0°$. A structured grid around this airfoil is generated, Figure 3, to calculate the fluid flow on different grid levels and with different order of finite elements, i.e. linear and quadratic Serendipity elements are considered here. The computational grid at level 0 as shown in Figure 3 is a C-type grid and consists of 561x81 points. On the airfoil, 401 points are distributed, whereas at the leading and trailing edge a grid spacing of 0.001 and 0.0006 was chosen.

The Mach number distribution of the fluid flow around the airfoil for the level 1 grid with bilinear quadrilateral elements using the discontinuous CBS scheme is shown in Figure 4(a). From the qualitative point of view this solution fits very well with that reported in [16]. The according pressure distribution is depicted in Figure 4(b). In Figure 4(c) the Mach number contours of the flow passing the airfoil are shown using biquadratic elements on the same grid level. The pressure distribution for the biquadratic element grid is shown in Figure 4(d). This solution shows better results compared with the solution given in [16], whereas both orders of interpolation use the same set of input parameters. A comparison of the discontinuous with continuous Galerkin CBS scheme is depicted in Figure 5 in terms of the surface pressure distribution for different grid levels and order of the spatial interpolation functions. As reference values, the surface pressure found in [16] and [17] are incorporated. As expected, better results are obtained with finer grids and higher order of the shape function interpolation, whereas only minor difference between the continuous and discontinuous Galerkin version of the CBS scheme could be observed.

Further it should be noted here, that for the continuous CBS scheme a consistent mass matrix is used to solve the systems of linear equations. With the current implementation of the algorithms and for the current flow problem, no improvement in the computational effort could be observed, when using the discontinuous Galerkin version of the CBS scheme compared to the continuous CBS scheme. Thus, the computational effort due to the additional edge flux evaluations within each step could not be compensated with the saving due to the omission of solving

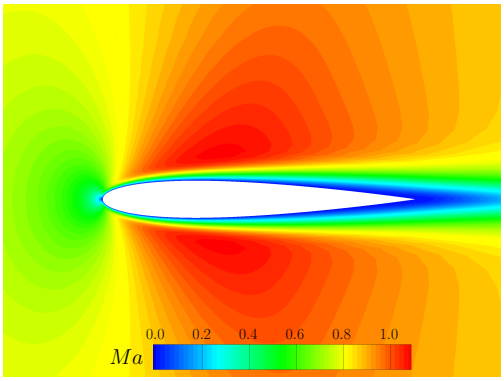


(a) Mach number contours - bilinear elements; level 1

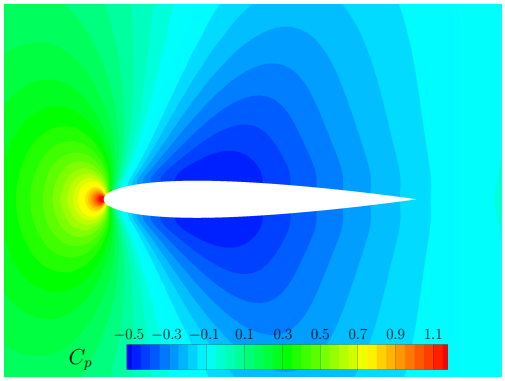


(b) pressure contours - bilinear elements; level 1

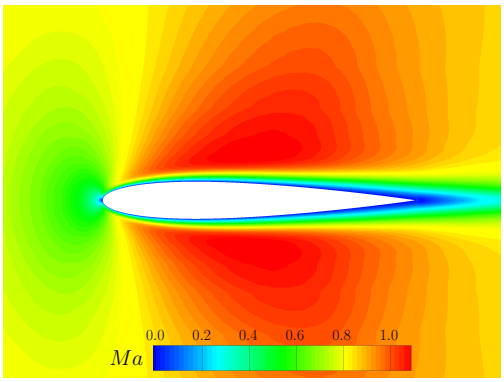


(c) Mach number contours - biquadratic elements; level 1

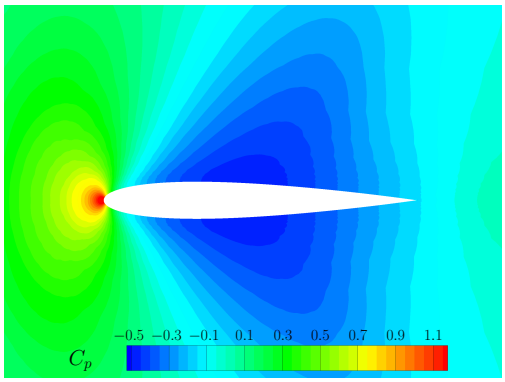


(d) pressure contours - biquadratic elements; level 1

Figure 4: Viscous flow past the NACA0012 airfoil at $Ma_\infty = 0.85$, $Re = 2000$ and $\alpha = 0°$ - Mach umber and pressure contours

a large system of linear equations. However, with grids involving more nodes, an improvement in the computational effort is likely to be observed, since the costs for the calculation of the edge flux varies linearly with number of nodes $N_m$, while the costs for solving a system of equations goes with $N_m^3$ (for the Gaussian elimination).

## 4 THREE-FIELD COUPLING APPROACH

For a coupled problem like a fluid flow interacting with a structure, a so-called three-field approach is used here, [18]. Both, the fluid and the structure, need to interchange data at an interface. Additionally, a frame is introduced to that each subdomain is connected only. The advantage of this three-field approach lies in the independent discretization of the frame, which allows a smooth data transfer across the interface by keeping the load and energy conservation property of the data transmission. In the context of the three-field approach the whole coupled

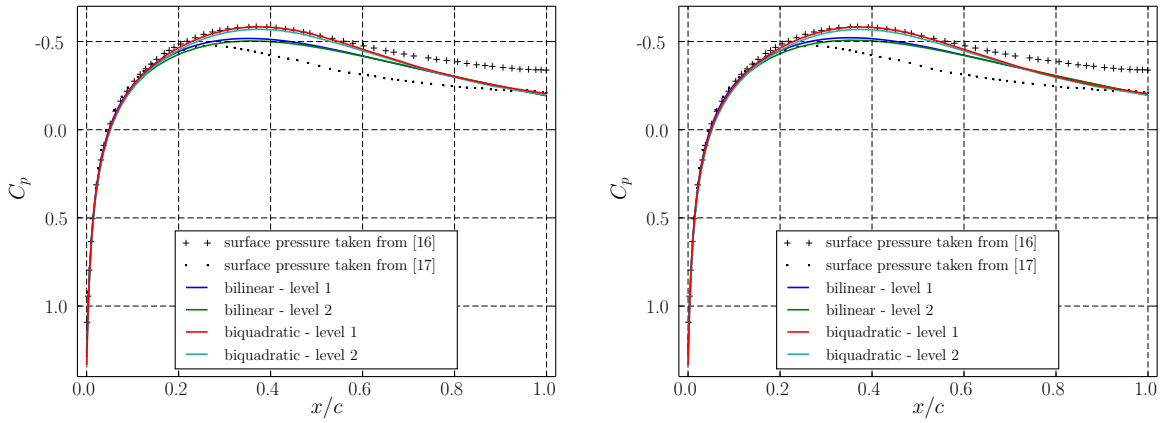


(a) continuous Galerkin version of the CBS scheme (b) discontinuous Galerkin version of the CBS scheme

Figure 5: Viscous flow past the NACA0012 airfoil at $Ma_\infty = 0.85$, $Re = 2000$ and $\alpha = 0°$ - surface pressure distribution

problem can be written in an operator-matrix form as:

$$\begin{array}{r} \text{Fluid:} \\ \text{Structure:} \\ \text{Transfer Fluid:} \\ \text{Transfer Structure:} \\ \text{Frame:} \end{array} \begin{bmatrix} \boldsymbol{\mathcal{F}} & 0 & \boldsymbol{\mathcal{M}}_{ff} & 0 & 0 \\ 0 & \boldsymbol{\mathcal{S}} & 0 & \boldsymbol{\mathcal{M}}_{ss} & 0 \\ \boldsymbol{\mathcal{M}}_{ff} & 0 & 0 & 0 & -\boldsymbol{\mathcal{M}}_{fc} \\ 0 & \boldsymbol{\mathcal{M}}_{ss} & 0 & 0 & -\boldsymbol{\mathcal{M}}_{sc} \\ 0 & 0 & -\boldsymbol{\mathcal{M}}_{cf} & -\boldsymbol{\mathcal{M}}_{cs} & 0 \end{bmatrix} \begin{bmatrix} \mathbf{u}_f^\Gamma \\ \mathbf{u}_s^\Gamma \\ \hat{\boldsymbol{\lambda}}_f \\ \hat{\boldsymbol{\lambda}}_s \\ \mathbf{u}_c \end{bmatrix} = \begin{bmatrix} \mathbf{0} \\ \mathbf{f}_s^\Gamma \\ \mathbf{0} \\ \mathbf{0} \\ \mathbf{0} \end{bmatrix} \tag{20}$$

where the fluid and structural operators $\boldsymbol{\mathcal{F}}$ and $\boldsymbol{\mathcal{S}}$ involve the computations of the fluid and structure subdomain, respectively. The nodal vectors $\mathbf{u}_f^\Gamma$, $\mathbf{u}_s^\Gamma$, $\hat{\boldsymbol{\lambda}}_f$ and $\hat{\boldsymbol{\lambda}}_s$ denotes the displacement field vector and the vector of discrete Lagrange multipliers on the fluid (subscript: $_f$) and structural (subscript: $_s$) interface $\Gamma$, respectively. The Lagrange multipliers $femvec\hat{\lambda}_i$ are defined on the the $i$th interface, i.e. they are localized on their respective interface representation, [19]. The vector $\mathbf{u}_c$ stands for the discrete frame displacement field (subscript: $_c$) and $\mathbf{f}_s^\Gamma$ are external nodal forces on the structure, which have other sources than the forces caused aerodynamically by the fluid. The coupling matrices are calculated by an integral statement as:

$$\boldsymbol{\mathcal{M}}_{ij} = \int_\Gamma \mathbf{N}_i^T \mathbf{N}_j \, d\Gamma \,, \tag{21}$$

The coupled system can be solved by a Richardson equilibrium iteration in each time step as:

$$\mathbf{u}_s^\Gamma = \boldsymbol{\mathcal{S}}^{-1} \circ (\mathbf{f}_s^\Gamma - \underbrace{\boldsymbol{\mathcal{M}}_{ss} \circ \boldsymbol{\mathcal{M}}_{cs}^{+\,T} \circ \boldsymbol{\mathcal{M}}_{cf}}_{\triangleq \boldsymbol{\mathcal{M}}_{sf}} \circ \boldsymbol{\mathcal{M}}_{ff}^{-1} \circ \boldsymbol{\mathcal{F}} \circ \boldsymbol{\mathcal{M}}_{ff}^{-1} \circ \underbrace{\boldsymbol{\mathcal{M}}_{fc} \circ \boldsymbol{\mathcal{M}}_{cs}^{+} \circ \boldsymbol{\mathcal{M}}_{ss}}_{\triangleq \boldsymbol{\mathcal{M}}_{fs} = \boldsymbol{\mathcal{M}}_{sf}^T} \circ \mathbf{u}_s^\Gamma) \,, \tag{22}$$

where it IS assumed that the number of fluid nodes on the interface is greater than the structural interface nodes. The matrix $\boldsymbol{\mathcal{M}}_{cs}^{+} = (\boldsymbol{\mathcal{M}}_{cs} \circ \boldsymbol{\mathcal{M}}_{sc})^{-1} \circ \boldsymbol{\mathcal{M}}_{\boldsymbol{cs}}$ denotes the Moore-Penrose

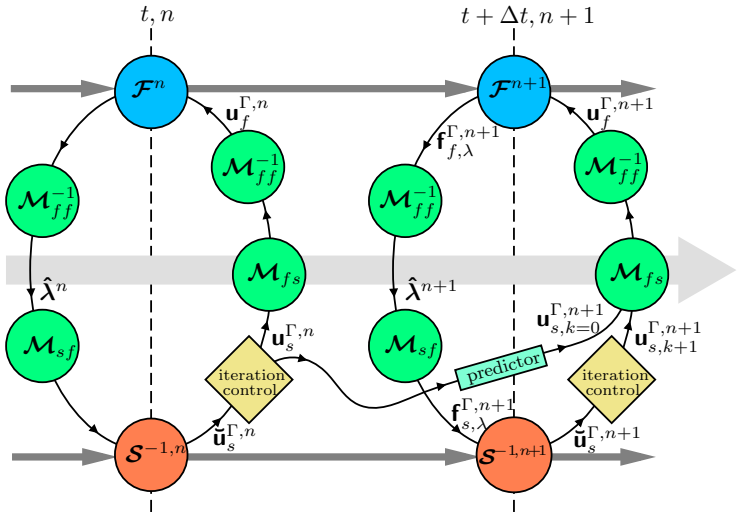


Figure 6: Time integration and equilibrium iteration for the coupled problem

pseudoinverse. Further it should be noted here, that the fluid is solved as a Dirichlet, whereas the structural subdomain is solved as Neumann problem. With this iteration procedure, the time integration and equilibrium iteration of the coupled problem can be illustrated as shown in Figure 6, where the time loop index is $n$ and the iteration index is $k$. For the vector $\mathbf{u}_{s,k=0}^{\Gamma,n+1}$ a second order time accurate predictor is used, [20]. Within the iteration control box a relaxation of the most recent computed structural displacement field $\breve{\mathbf{u}}_s^{\Gamma,n+1}$ is conducted.

## 5 PANEL FLUTTER PROBLEM

The typical non-linear and dynamic aeroelastic phenomenon of the panel flutter is investigated with the aid of schemes presented in previous sections. This classical aeroelastic problem often used as an aeroelastic model problem exhibit a limit cycle oscillation (LCO), i.e. the flutter amplitude is restricted due to the non-linear nature of the thin structure.

### 5.1 Problem description and aeroelastic parameters

The panel flutter problem consists of a simply supported plate over which a fluid flows, Figure 7. Due this fluid flow, the panel can exhibit a self-exciting oscillation - a flutter phenomenon. Usually the plate or panel is very thin and has therefore to be modeled as a non-linear structure, which leads to a restriction of the flutter amplitude (limit cycle oscillation). The occurrence of such LCO depends on the combination of parameters like the panel thickness, the flow Mach number or the flow pressure at infinity.

To take the large structural deformation into account, the panel itself is modeled with the von Kármán plate model, where the non-linearity comes from an in-plane restoring force, whose value depends on the panel deflection, [21, 22]. Here, the structural system is spatially discretized by Timoshenko beam elements, which are free of shear locking, resulting in the following matrix

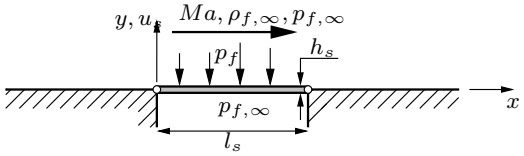


Figure 7: Description of the panel flutter problem

system, [23, 24]:

$$\left[(\rho_s h_s)\mathbf{M}_u + \frac{\rho_s h_s^3}{12}\mathbf{M}_\theta\right]\ddot{\mathbf{u}}_s + \left[D\mathbf{K}_u + \tfrac{5}{6}Gh_s\mathbf{K}_\theta + \tfrac{1}{2}Eh_s(\mathbf{u}_s^T\mathbf{K}_R\mathbf{u}_s)\mathbf{K}_R\right]\mathbf{u}_s = \mathbf{f}_{u,\text{ext}}\,, \tag{23}$$

where the values $D$ and $G$ denotes the plate stiffness and shear module of the panel with:

$$D = \frac{Eh_s^3}{12(1-\nu_s^2)}; \qquad G = \frac{E}{2(1+\nu_s)}; \tag{24}$$

with $E$ and $\nu_s$ being the Young's modulus and the Poisson's ratio of the panel, respectively. The non-linearity is given by the third part of the stiffness term in Eq. (23). For a definition of the matrices $\mathbf{M}_u$, $\mathbf{M}_\theta$, $\mathbf{K}_u$, $\mathbf{K}_\theta$ and $\mathbf{K}_R$ consult [23, 24].

The structural parameters like panel length $l_s$, thickness $h_s$, stiffness and the fluid parameters like density, pressure and velocity of the flowing air at infinity can be expressed through three aeroelastic parameters.

1. non-dimensional mass ratio $r_m$:

$$r_m = \frac{\rho_{f,\infty} l_s}{\rho_s h_s} = \frac{\rho_{f,\infty}}{\rho_s \frac{h_s}{l_s}} \tag{25}$$

2. non-dimensional dynamic pressure $r_p$:

$$r_p = \frac{\rho_{f,\infty} v_{f,\infty}^2 l_s^3}{D} = \frac{\rho_{f,\infty} v_{f,\infty}^2 12(1-\nu_s^2)}{E\left(\frac{h_s}{l_s}\right)^3} \tag{26}$$

3. reduced frequency $K$

$$K = \frac{\pi f l_s}{v_{f,\infty}}\,, \tag{27}$$

Here, the reduced frequency is the result of the computation for the panel flutter problem and therefore the Mach number $Ma_\infty$ is used as third input parameter. Thus, the aeroelastic problem of the panel flutter is defined by the three input parameter $(r_m, r_p, Ma_\infty)$. Given a panel with the material density $\rho_s$, Young's modulus $E$ and Poisson's ratio $\nu_s$ as well as the geometric parameters $h_s$ and $l_s$, the fluid density velocity at infinity are obtained from Eq. (25) and (26), respectively.

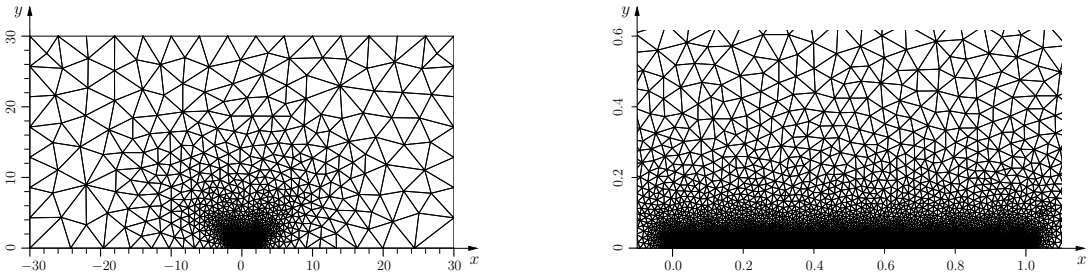


(a) full grid

(b) close-up view on the panel

Figure 8: Unstructured grid for calculations of inviscid panel flutter problem

### 5.2 Transonic Panel Flutter

The panel flutter problem is investigated at a transonic Mach number of $Ma_\infty = 1.0$. The panel is made by aluminum with a density of $\rho_s = 2700\,\mathrm{kg/m^3}$, a Young's modulus of $E = 7.1 \cdot 10^{10}\,\mathrm{N/m^2}$ and Poisson's ratio of $\nu_s = 0.34$. The geometry of the panel is set to a thickness of $h_s = 4.537\,\mathrm{mm}$ and a length of $l_s = 1.0\,\mathrm{m}$ and the panel is simply supported at $x/l_s = 0.0$ and $x/l_s = 1.0$

In [25] a bifurcation of the panel's aeroelastic behavior with a constant mass ratio of $r_m = 0.1$ was reported when increasing the non-dimensional dynamic pressure $r_p$ from 160 to 180. At a pressure of $r_p = 180$ a limit cycle oscillation can be observed and for $r_p = 160$ a divergence of the panel is predicted. For a pressure of $r_p = 170$ flutter should be observed and therefore this case is chosen as a testcase. For this testcase, an inviscid fluid is assumed and therefore the Euler equations of the fluid motion are solved.

#### 5.2.1 Principal flutter behavior

In a first initial verificational computation, a triangular unstructured grid is used as depicted in Figure 8. This grid consists of 7516 nodes connected to 14521 elements. In the vicinity of the panel ($0.0 \leq x \leq 1.0$) small elements were placed, Figure 8(b), and the fluid interface is discretized with 400 elements.

For the calculations presented in this section a constant time step of $\Delta t = 10^{-3}\,\mathrm{s}$ is used. A simple staggered scheme, where one data exchange is conducted in each time step, is used here in conjunction with a second order predictor for the structural displacements. The structure itself is discretized with 100 elements. Further, in terms of the CBS scheme, the explicit scheme with $\theta_1 = 0.75$ and $\theta_2 = 0.0$ was applied as well as the consistent mass matrix within the CBS scheme was used.

In Figure 9, the midpoint deflection of the panel using both - the continuous and discontinuous - version of the CBS scheme is depicted. Both methods show a similar dynamic panel behavior. The time history is non-dimensionalized with $\pi l_s / v_{f,\infty}$ so that the reduced period time $1/K$ can be directly identified from the time history plots. With a continuous CBS scheme a reduced frequency of $K = 0.116$ could be computed whereas the frequency for the discontinuous version is 0.113. The flutter amplitudes were $(u_s/h_s)_{x/l_s=0.5} = 1.72$ and 1.70 for the continuous and

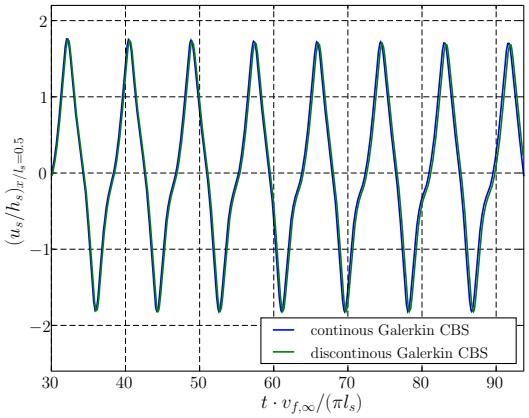


Figure 9: Midpoint deflection of the panel using continuous and discontinuous version of CBS scheme - time step size $\Delta t = 0.001\,\mathrm{s} \Rightarrow \Delta t \cdot v_{f,\infty}/(\pi l_s) = 0.094$

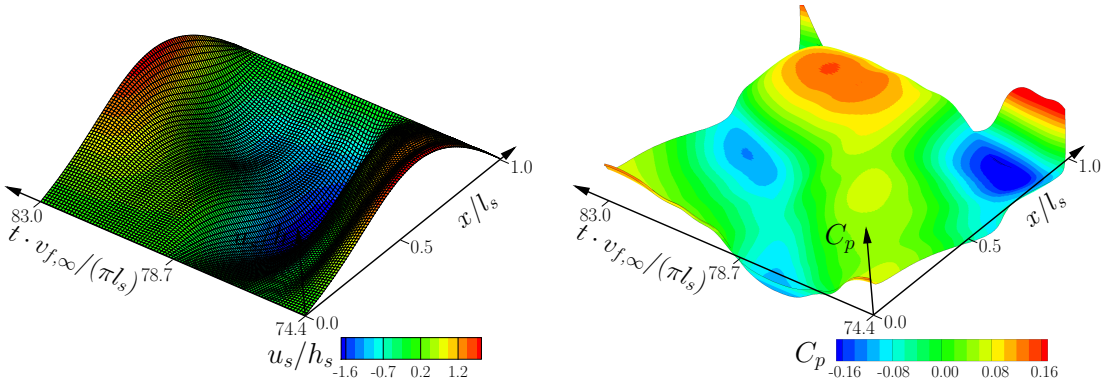


(a) panel deformation (b) pressure coefficient

Figure 10: Deformation of the panel during one cycle of oscillation and the according pressure load on the panel using discontinuous version of CBS scheme

discontinuous CBS scheme, respectively. These results fit very well with those reported in [25], where a reduced frequency of 0.108 and a non-dimensional amplitude of 1.79 was obtained.

The deflection of the panel over one period of the limit cycle oscillation is shown in Figure 10(a), where the panel deformation is also colored. The panel is fully deflected in positive $y$-direction at a non-dimensional time $t \cdot v_{f,\infty}/(\pi l_s) = 74.4$. The structure then rapidly deflects to the opposite direction. From the bottom dead center the panel is now deformed to the top dead center, while the deflections show a wavelike behavior, where the first 50% of the panel reaches a positive deflection at $t \cdot v_{f,\infty}/(\pi l_s) \approx 79.0$ before the remaining panel part follows upward. The corresponding pressure coefficient on the fluid discretization of the interface is shown in Figure 10(b), where a weak shock occurs on the panel, which is mostly present while the panel deforms from bottom to the top dead center. This shock moves from middle to the end of the panel and the Galerkin based transfer is able to resolve this shock while the pressure distribution is transmitted from a fine fluid interface grid to the structural interface representation.

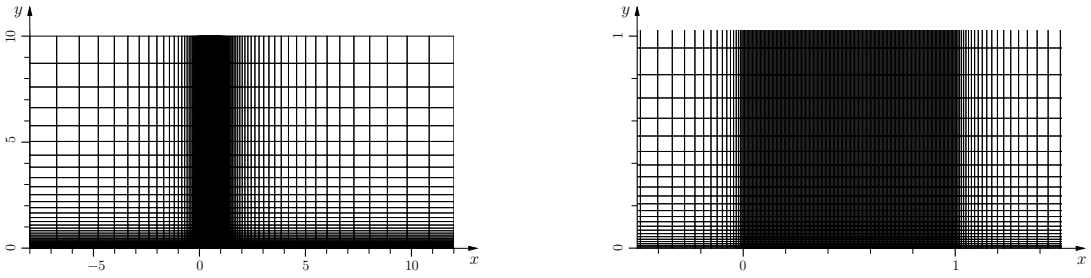


(a) full grid (b) close-up view on the panel

Figure 11: Example of a structured grid for calculations of inviscid panel flutter problem - 160 elements distributed on the panel

### 5.2.2 Convergence study on structured grids

According to section 3, a structured grid is now used for the panel flutter problem, due to its simple creation of similar grids with bilinear or biquadratic finite elements at different grid refinement levels. In Figure 11, an example of a structured grid is shown, which is characterized by the existence of 160 elements distributed on the panel. Other discretizations created for the computations use 80, 120, 240 or 320 elements on the panel. Here again the panel flutter phenomenon is computed with the same parameter set as described above ($Ma_\infty = 1.0$, $r_m = 0.1$, $r_p = 170$).

| | **CBS scheme** | |
|---|---|---|
| | continuous | discontinuous |
| 80 linear elements: | 0.1686 | 0.1651 |
| 160 linear elements: | 0.1376 | 0.1369 |
| 240 linear elements: | 0.1192 | 0.1187 |
| 320 linear elements: | 0.1090 | 0.1088 |
| 80 quadratic elements: | 0.1522 | 0.1518 |
| 120 quadratic elements: | 0.1121 | 0.1117 |

Table 1: Reduced frequency of the limit cycle oscillation using different versions of the CBS scheme and number of elements on the interface

In Figure 12, the midpoint deflection together with the midpoint velocity is shown for different discretizations and for different spatial order of finite elements. Using coarse grid with bilinear elements and with 80 elements on the interface, a high flutter frequency of 0.1686 and 0.1651 for both versions of the CBS scheme are obtained, Table 1. Comparing these results with a finer grid, e.g. 320 elements at the interface Figure 12(d), this high frequency is caused by a non-satisfying midpoint velocity time history. While the panel moves to the top dead center,

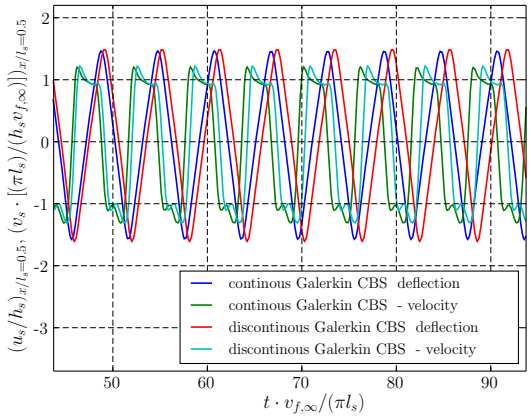


(a) 80 linear elements on the fluid interface

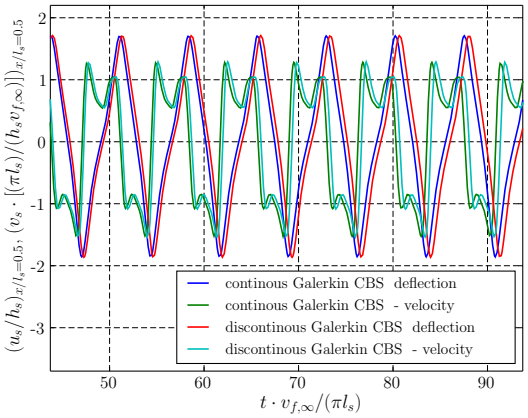


(b) 160 linear elements on the fluid interface

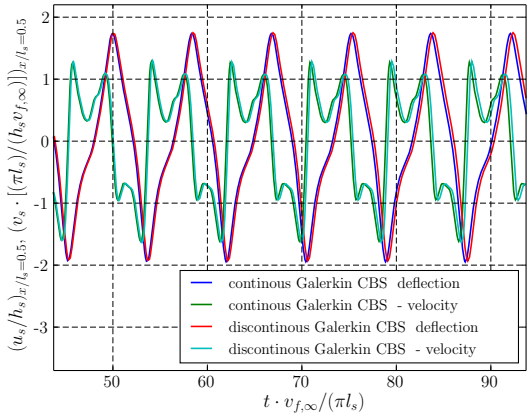


(c) 240 linear elements on the fluid interface

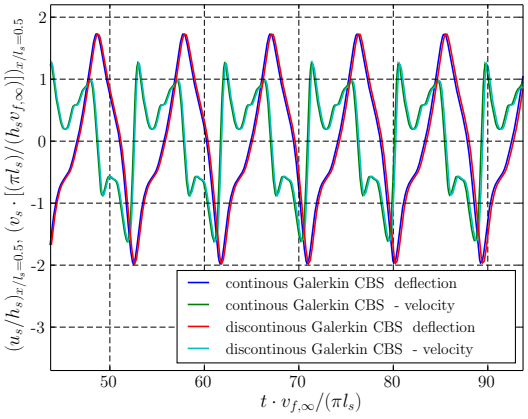


(d) 320 linear elements on the fluid interface

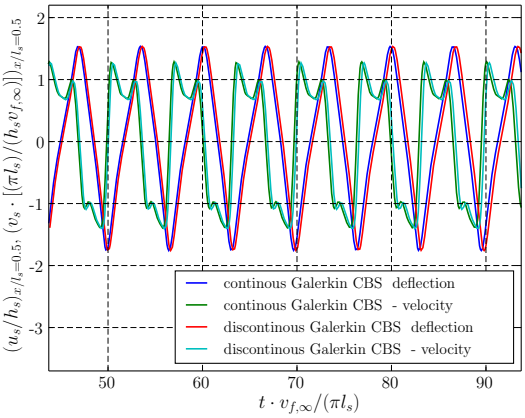


(e) 80 quadratic elements on the fluid interface

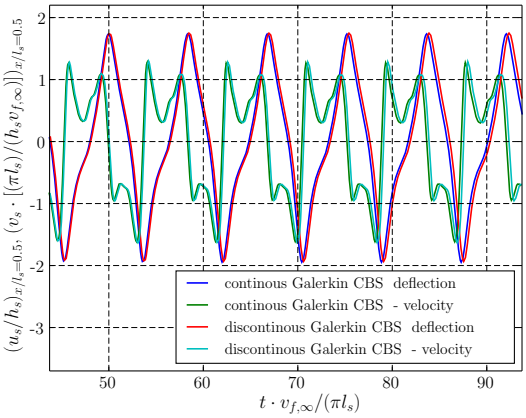


(f) 120 quadratic elements on the fluid interface

Figure 12: Midpoint deflection of the panel using different version of CBS scheme and number of elements at the fluid interface

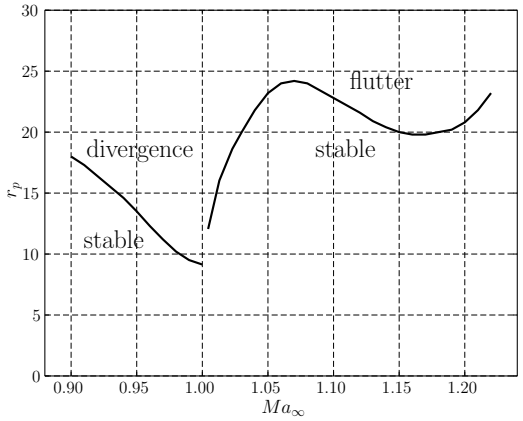


Figure 13: Stability boundary of a simply supported panel at $r_m = 0.1$

the velocity shows a higher mode, where the midpoint velocity almost reaches zero. Further, from Table 1 it can be seen, that with more linear elements, the flutter frequency is reduced to the value reported in [25], where the difference between the continuous and the discontinuous Galerkin CBS scheme also is reduced with finer grids.

Using grids with biquadratic elements, similar expressions can be made. Although better results could be obtained when using 80 elements at the fluid interface, the velocity time history of the midpoint deflection is still insufficient. With 120 quadratic elements at the interface, the obtained reduced frequency lies between that obtained with grids where 240 and 320 linear interface elements were used. This confirms the observation known from finite element analysis, that a p-refinement converges better than a h-refinement of the grid.

Finally, the stability boundary chart of the panel is depicted in Figure 13, where the computations were carried out with the discontinuous version of the CBS scheme. Here it can be seen, that with a Mach number of $Ma_\infty < 1.0$ the stability boundary divides the $Ma - r_p$-plane into an area with divergence and an area with stable flutter behavior. For a Mach number $Ma_\infty > 1.0$, the $Ma - r_p$-plane is divided into areas with a stable and with an unstable flutter behavior. This results fits very well with those obtained in [26].

## 6 CONCLUSIONS

In this paper the applicability of the CBS scheme for problems in fluid structure interaction was verified. Contrary to the finite volume method, one major drawback of the standard CBS scheme is its non-local conservation property. In this paper, a discontinuous Galerkin version of the CBS scheme was employed for the Navier-Stokes equation in the ALE frame of reference. This discontinuous Galerkin version has three advantages: first, the flux crossing two adjacent elements can explicitly set equal, second, for cases where a lumped mass matrix is disadvantageous to use, the discontinuous Galerkin version can be utilized to avoid solving a large system of linear algebraic equations, and third the changes in the code implementation are small and only a few extra methods are needed.

The discontinuous Galerkin CBS scheme was verified for the laminar flow around the standard NACA0012 airfoil for different grid levels and spatial order of finite elements, where only

small differences between the continuous and discontinuous version could be observed. As an aeroelastic example, the classical panel flutter problem was chosen. Here, the differences in the obtained flutter frequency are again small, although slightly better results could be obtained with the discontinuous Galerkin CBS scheme.

## REFERENCES


[1] O.C. Zienkiewicz and Y.K. Cheung. Finite elements in the solution of field problems. *The Engineer*, 220:507–510, 1965.

[2] J.T. Oden. *Finite elements of nonlinear continua*. McGraw-Hill, 1972.

[3] T. J. Chung and J. N. Chiou. Analysis of unsteady compressible boundary layer flow via finite elements. *Computers and Fluids*, 4:1–12, 1976.

[4] O.C. Zienkiewicz and R. Codina. A general algorithm for compressible and incompressible flow - part i. the split characteristic-based scheme. *International Journal for Numerical Methods in Fluids*, 20(8-9):869–885, 1995.

[5] O.C. Zienkiewicz, K. Morgan, B.V.K.S. Sai, R. Codina, and M. Vasquez. A general algorithm for compressible and incompressible flow - part II. tests on the explicit form. *International Journal for Numerical Methods in Fluids*, 20(8-9):887–913, 1995.

[6] P. Nithiarasu, R. Codina, and O.C. Zienkiewicz. The Characteristic-Based split (CBS) scheme-a unified approach to fluid dynamics. *International Journal for Numerical Methods in Engineering*, 66(10):1514–1546, 2006.

[7] O.C. Zienkiewicz, R.L. Taylor, and P. Nithiarasu. *The finite element method for fluid dynamics*. Elsevier Butterworth-Heinemann, Amsterdam, 6th ed. edition, 2005.

[8] C.G. Thomas. *A locally conservative Galerkin (LCG) finite element method for convection-diffusion Navier-Stokes equation*. PhD thesis, University of Wales, School of Engineering, 2006.

[9] C.G. Thomas, P. Nithiarasu, and R.L.T. Bevan. The locally conservative galerkin (LCG) method for solving the incompressible Navier-Stokes equations. *International Journal for Numerical Methods in Fluids*, 57(12):1771–1792, 2008.

[10] B. Cockburn. Discontinuous galerkin methods. *ZAMM*, 83(11):731–754, 2003.

[11] B.Q. Li. *Discontinuous finite elements in fluid dynamics and heat transfer*. Springer, 2006.

[12] T.J.R. Hughes, G. Scovazzi, P.B. Bochev, and A. Buffa. A multiscale discontinuous galerkin method with the computational structure of a continuous galerkin method. *Computer Methods in Applied Mechanics and Engineering*, 195(19-22):2761–2787, 2006.

[13] J. Iannelli. *Characteristics finite element methods in computational fluid dynamics*. Springer, 2006.

[14] A. Jameson. Time dependent calculations using multigrid with application to unsteady flows past airfoils and wings. *AIAA-Paper 91-0596*, 1991.

[15] C. Farhat, P. Geuzaine, and C. Grandmont. The discrete geometric conservation law and the nonlinear stability of ALE schemes for the solution of flow problems on moving grids. *Journal of Computational Physics*, 174(2):669–694, 2001.

[16] S. Mittal. Finite element computation of unsteady viscous compressible flows. *Computer Methods in Applied Mechanics and Engineering*, 157(1-2):151–175, 1998.

[17] L. Cambier. Computation of viscous transonic flows using an unsteady type method and a zonal grid refinement technique. In *Numerical Simulation of Compressible Navier Stokes Flows*, volume 18 of *Notes of Numerical Fluid Mechanics*, 1987.

[18] R. Unger, M.C. Haupt, and P. Horst. Application of lagrange multipliers for coupled problems in fluid and structural interactions. *Computers & Structures*, 85(11-14):796–809, 2007.

[19] K.C. Park and C.A. Felippa. A variational principle for the formulation of partitioned structural systems. *International Journal for Numerical Methods in Engineering*, 47(1-3):395–418, 2000.

[20] S. Piperno. Explicit/implicit fluid/structure staggered procedures with a structural predictor and fluid subcycling for 2D inviscid aeroelastic simulations. *International Journal For Numerical Methods In Fluids*, 25(10):1207–1226, 1997.

[21] E. H. Dowell. *Aeroelasticity of plates and shells.* Noordhoff International Publishing, 1975.

[22] R. Clark and E. H. Dowell. *A modern course in aeroelasticity.* Kluwer Academic Publishing, 2004.

[23] J. Hurka. *Numerische Untersuchung zur Aerolastik duenner Platten.* PhD thesis, RWTH Aachen, 2001.

[24] Z. Friedman and J.B. Kosmatka. An improved two-node timoshenko beam finite element. *Computers & Structures*, 47(3):473–481, 1993.

[25] R. Massjung. *Numerical schemes and well posedness in nonlinear aeroelasticity.* PhD thesis, RWTH Aachen, 2002.

[26] G. Davis and O. O. Bendiksen. Transonic panel flutter. *AIAA-Paper 93-1476*, 1993.